

# **Supplementary Materials for ‘Spatial plus Wavelet Dual-domain Empowering High-quality Electrical Impedance Tomography Reconstruction’**

Zichen Wang, *Member, IEEE*, Tao Zhang, *Graduate Student Member, IEEE*, Xinyu Zhang,

Yang Xiao, *Fellow, IEEE*, Qi Wang, *Member, IEEE*<sup>1</sup>

**Abstract-** In the supplementary materials, we provide more information of datasets and comprehensive results that do not illustrate in the main manuscript. The visualizations and metrics are both listed, and some additional experiments are also given in this attachment.

**Index terms:** EIT, dual-domain features, Fourier convolution, wavelet Transformer, inverse problem.

## I 、 Datasets:

The observation area is set a circular shape with the diameter of 0.19 m, and there are 16 electrodes uniformly attached on the outside boundary of the domain. The protocol of data acquisition is ‘adjacent current excitation-adjacent voltage measurement’, where the current is utilized with the amplitude of 4.5 mA and the frequency of 50kHz. The NaCl solution with 0.06 S/m is set up as background in the homogeneous field. The forward problem of EIT is solved by finite elements method (FEM), the observation domain is discretized into a triangular mesh and then solved. For the 16-electrode EIT measurement model, a total of 208 voltages are obtained for all electrodes excitation-measurement at one time. In order to avoid the problem of ‘inverse crime’, different discrete meshes are used to characterize the conductivity distribution in the domain. The observation

---

<sup>1</sup> This Manuscript received on Month, Date, 2025, revised on XXXX. Manuscript ID: Journal name-No-Year.

This work was supported by National Natural Science Foundation of China (NSFC) under Grant 62072335, Grant 62071328, Grant 61872269 and Grant 61903273, Key project of Tianjin Natural Science Foundation (24JCZDJC00790), and also supported by Tianjin Key Laboratory of Optoelectronic Detection Technology and System (LODTS) No. 2024LODTS203. (Corresponding authors: Qi Wang ([wangqitju@163.com](mailto:wangqitju@163.com)), Zichen Wang ([wangzc@tiangong.edu.cn](mailto:wangzc@tiangong.edu.cn))).

Zichen Wang, Tao Zhang, Qi Wang are with the School of Electronic and Information Engineering, and also with the Tianjin Key Laboratory of Optoelectronic Detection Technology and System, Tiangong University, Tianjin 300387, China. (Author email: [wangzc@tiangong.edu.cn](mailto:wangzc@tiangong.edu.cn), [zhangtao@tiangong.edu.cn](mailto:zhangtao@tiangong.edu.cn), [wangqitju@163.com](mailto:wangqitju@163.com).)

Xinyu Zhang and Yang Xiao are with the Department of Computer Science, The University of Alabama, Tuscaloosa, AL 35487 USA (e-mail: [xzhang205@crimson.ua.edu](mailto:xzhang205@crimson.ua.edu), [yangxiao@ieee.org](mailto:yangxiao@ieee.org)).

This is the supplemental materials of the main paper submitted to IEEE TCSV.

Color versions of one or more of the figures in this article are available online at <http://ieeexplore.ieee.org>

domain is divided using square grids into  $256 \times 256$  pixels to adequately represent information about inclusions with complex boundary shapes.

*(1) Multi-phase inclusion distributions:* The inclusions with multi-phase distributions with the conductivity in the range of  $10^{-6}$ - $10^6$  S/m. The radius is set in the range of 0.02-0.08m, the number of inclusions is set as from 1 to 4. These inclusions do not intersect each other. A total of 52,430 (containing 42,430 circle inclusions and 10,000 shaped inclusions) simulation samples are obtained. The training, validation and test samples are set to be 80%, 10% and 10% of the total database respectively.

*(2) Healthy/injured lung-phantoms:* The structured information of the human chest is obtained according to the CT image, and the process of constructing simulation models is described in the literature. The conductivities of healthy organs are set as: fat with 0.30 S/m, heart with 0.50 S/m, aorta with 0.60 S/m, spine with 0.09 S/m, and the inflated lung with 0.15 S/m. The lung injury is simulated by randomly removing a portion of the lungs and replacing the missing portion with the other medium, where the conductivity of the injured lungs ranges from 0.165 to 0.285 S/m. For augmenting the simulation data, the Gaussian white noise is added to the measurements with a signal-to-noise ratio (SNR) of 65 dB. Finally, the number of simulated lung phantoms is 9,100 for training and 1,000 for testing, respectively.

## II、NOISE ROBUSTNESS ANALYSIS:

In this subsection, two different noisy perturbations are mainly considered for evaluating the robustness of our SpW-Net and competing methods.

*(1) Measurement noise:* To evaluate the robustness of SpW-Net under different levels of noise, a series of Gaussian white noise is added to the simulation test dataset, in which the SNR levels for these additive noises are set in the range from 70 to 20 dB. The robustness of our SpW-Net and four learning-based models (SWISTA-Net, IDT, DnSwin, and EWT) is compared separately. We evaluate the performance of SpW-Net and methods using average PSNR and SSIM on various noise levels, and the results are shown in Fig. S1.

It can be seen that the performance of all methods decreases as the SNR level decreases, SpW-Net outperforms the other methods in terms of both PSNR and SSIM for all levels of noise. In detail, the RMSE is lower than 5.0 as well as SSIM is higher than 0.95 of SpW-Net when the SNR is lower than 40 dB. Due to the test model being trained under the noise-free datasets, these results indicate that our SpW-Net with spatial and wavelet hybrid domains could effectively suppress the artifacts due to systemic perturbations. Moreover, the multi-scale and low/high-frequency sub-band fusion strategies in SpW-Net could enhance the valuable information describing the conductivities and shape features simultaneously.

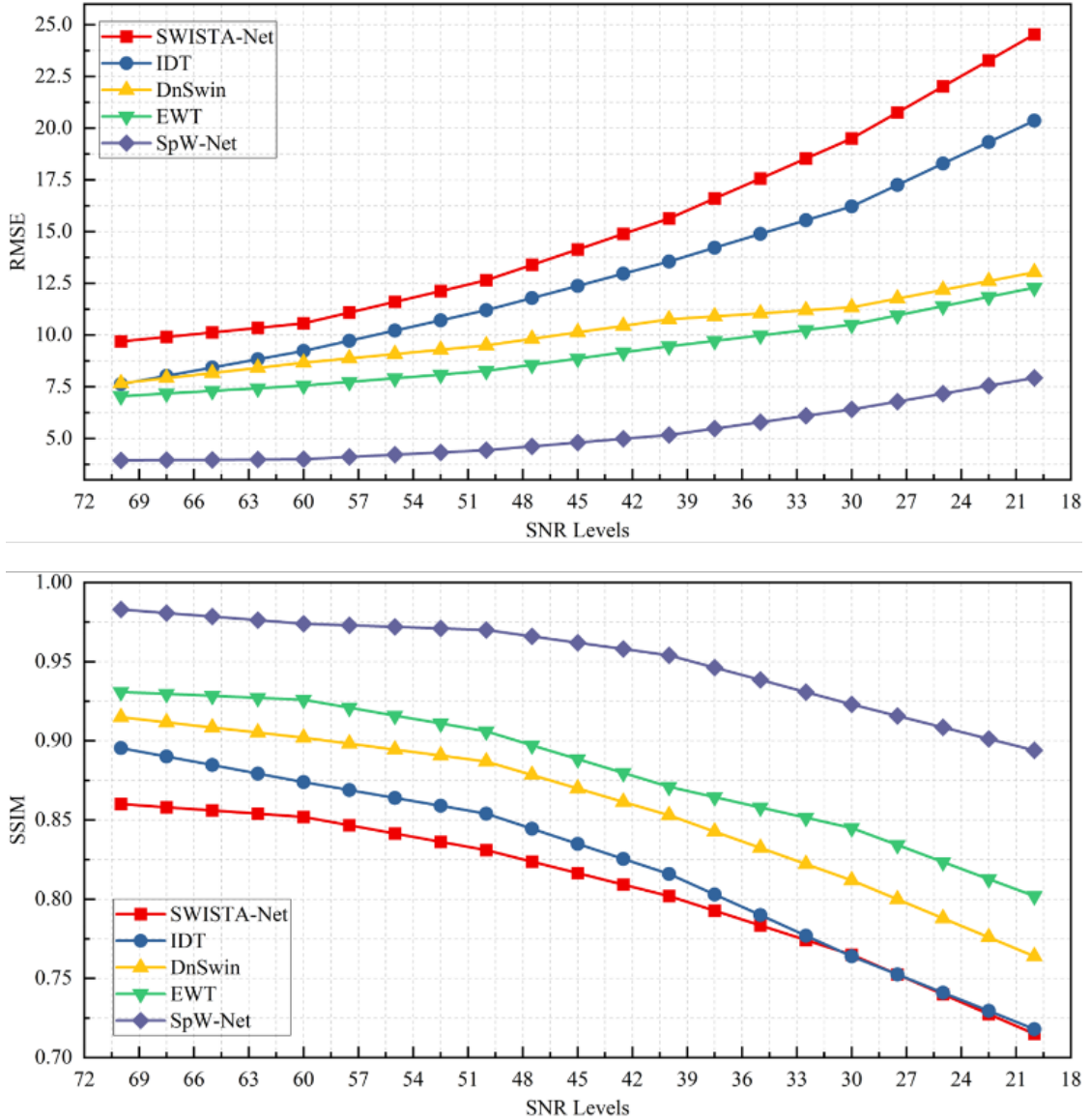


Figure S1 The noise robustness analysis (quantitative metrics of RMSE and SSIM) under different Gaussian noise SNR-levels.

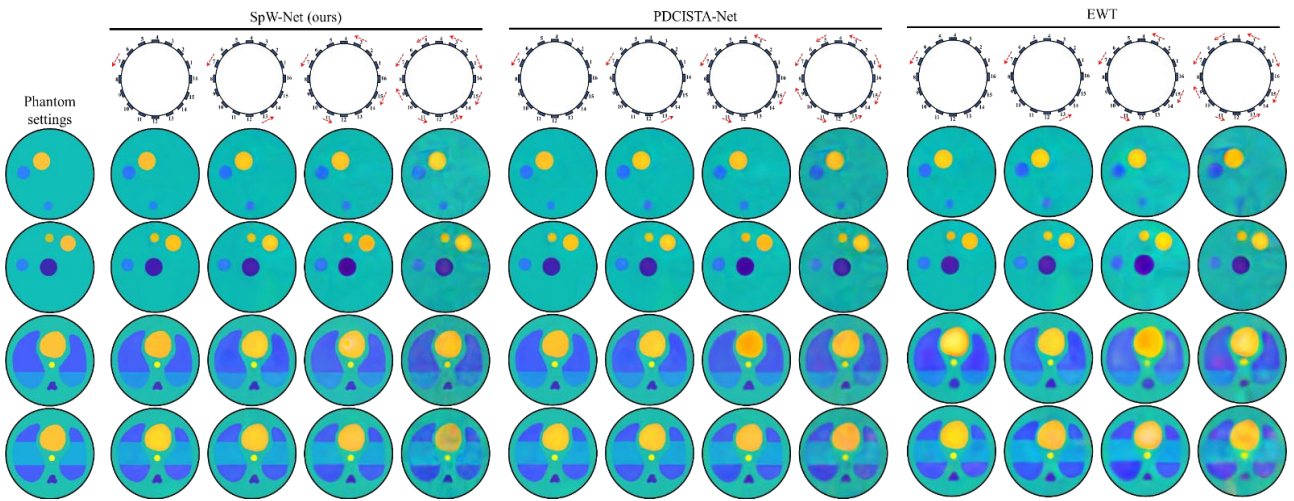


Figure S2 Visual reconstructions of electrode movements experiment for validation in the noise robustness. In these experiments, we consider the one-, two-, four-, and eight-electrode movements tasks (shown in the first row), and four cases (two shape reconstructions and two lung phantoms) are considered using the SpW-Net method and PDCISTA-Net, EWT for comparison.

(2) *Electrode movements*: Some other perturbations have to be considered for addressing practical noise issues, such as the electrode movement that may occur in medical applications. In this paper, the 1, 2, 4, and 8 electrodes random movements are considered, respectively. To better illustrate the results, our SpW-Net is compared with two SOTA imaging methods including PDCISTA-Net and EWT. The visual reconstructions are shown in Figure S2.

The visual perceptions in Figure S2 show that our SpW-Net has more robust performances under different electrode movements. The major reasons include (1) the learnable pre-reconstruction is introduced in wavelet-domain, which couples the VFM features with spatial locations of sensor placements, (2) the spatial and wavelet domains could enhance the focused inclusions as well as suppress the artifacts, which highlight the high-frequency sub-bands and the final results have sharper boundary features.

### III. COMPREHENSIVE RESULTS

In this section, the comprehensive experimental results are shown including the multi-phase inclusions and lung-shaped phantoms. Moreover, some representative analyses are illustrated.

To compare the performance of SpW-Net, we use three broad approaches to compare: CNN-based methods, unrolling-based frameworks, and Transformer-based approaches.

a) *CNN-based methods*: Our comparative experiments are carried out by CNN-based end-to-end architectures including VA-Net [1], EED [2], DHU-Net [3]. These have been proposed to improve reconstruction performance by incorporating attention or advanced convolution mechanisms.

b) *Unrolling-based frameworks*: Meanwhile, several model-based unrolling frameworks are utilized as the major contenders, including FISTA-Net [4], SWISTA-Net [5], PDCISTA-Net [6], which embed the physical prior to improve the imaging results and generalizations.

c) *Transformer-based and dual-domain approaches*: Moreover, the Transformer module with spatial and wavelet-domain methods, i.e. SwinIR [7], Restormer [8], UFormer [9], DnSwin [10], DRSFormer [11], IDT [12], MWDCNN [13], WSDFormer [14], EWT [15], DECS-Net [16], are regarded as important methodologies for comparison.

For the competing methods, the implementations are downloaded from their respective websites and performed based on their defaults. To ensure fair comparisons, all these competing methods are re-trained using the same datasets on the same environments.

#### A. Simulated data results:

In Figures S3 to S6, the more representative reconstructions are shown, where the visual results and absolute error maps are shown. The absolute error maps between reconstructions and ground truth to could highlight the differences in visual perceptions and display the texture details. As shown in these two groups of visualizations and error maps, the proposed SpW-Net is capable of

reconstructing clearer and sharper boundaries and accurate electrical distributions.

*B. Experimental data results:*

In this subsection, a circular tank with 16 electrodes is used for real-world experiments. The multiphase conductivity distributions are performed utilizing food materials (cucumber, carrot, and sugarcane and injected with different concentrations of NaCl solution to change the conductivity of the materials), as well as the healthy/injured medical reconstructions are performed using lung-shaped phantoms made from agar with different conductivities. The water with a conductivity value of 0.6 S/m is used as a homogeneous background, and different inclusions are placed in the tank to set as the inhomogeneous states for obtaining the measured voltages. The two experimental results, i.e. multi-phase inclusions distributions and lung-shaped phantoms, are shown in Figures S7 and S8.

*C. Impedance resolution analysis:*

Figure S9 shows the horizontal/vertical profiles. The results demonstrate that the SpW-Net achieves promising gains in terms of the resolution preservation (especially the impedance resolution) than the other competing methods do.

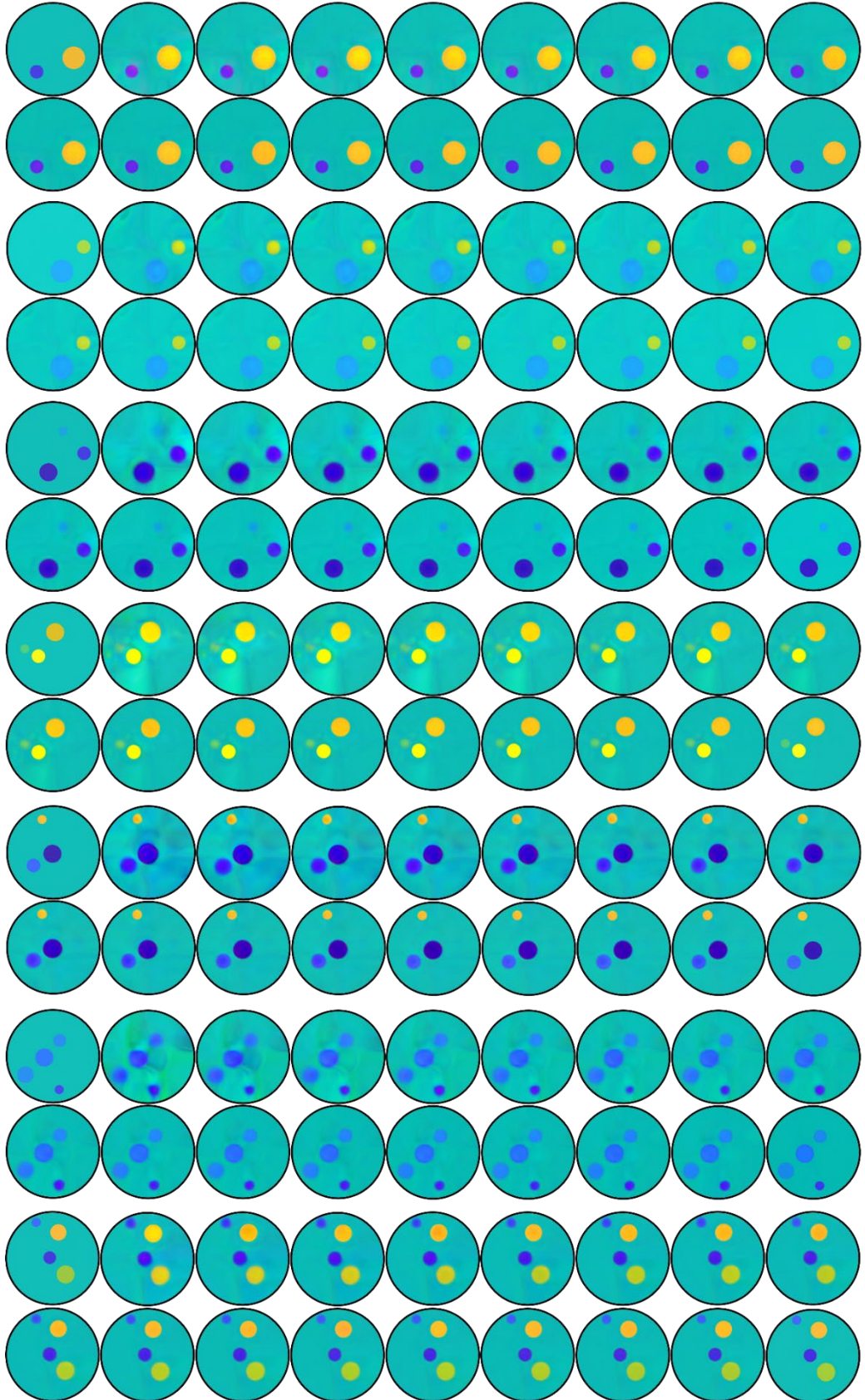


Fig. S3 The **visualizations** of reconstruction results under the *multi-phase inclusions distributions of simulated test datasets*. In each group, the first and second row indicate the reconstructed images, and the third and fourth row show the absolute error maps between the reconstruction and the ground truth. Here, the first image shows the ground truth distribution, and the last image shows the results of our SpW-Net, respectively. The other images are results of different comparisons including FISTA-Net, VA-Net, EED, DHU-Net, SWISTA-Net, PDCISTA-Net, SwinIR, Restormer, UFormer, IDT, DnSwin, DRSFormer, MWDCNN, WSDFormer, EWT, DECS-Net.

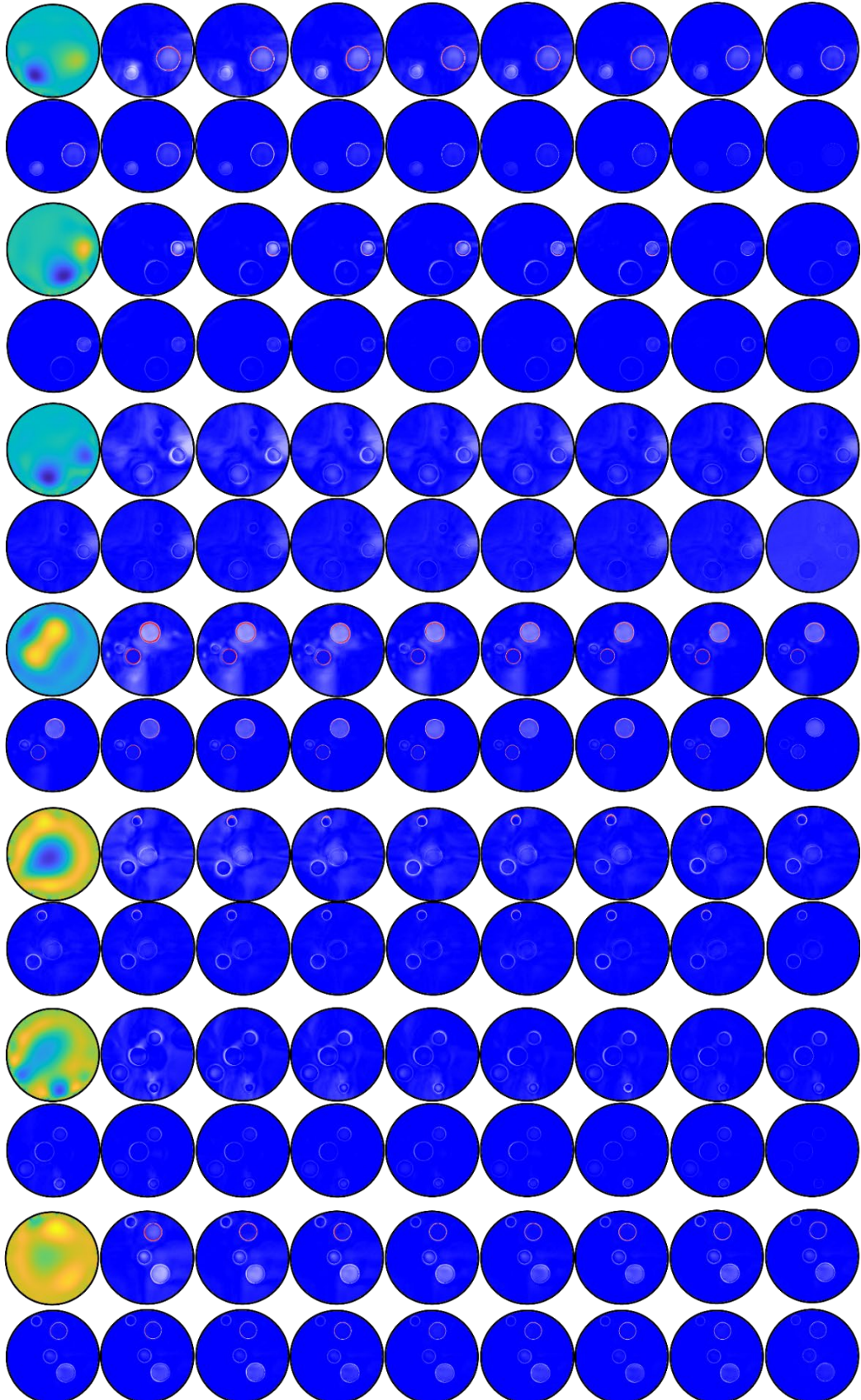


Fig. S4 The **absolute error maps** of reconstruction results under the **multi-phase inclusions distributions of simulated test datasets**. In each group, the first and second row indicate the reconstructed images, and the third and fourth row show the absolute error maps between the reconstruction and the ground truth. Here, the first image shows the ground truth distribution, and the last image shows the results of our SpW-Net, respectively. The other images are results of different comparisons including FISTA-Net, VA-Net, EED, DHU-Net, SWISTA-Net, PDCISTA-Net, SwinIR, Restormer, UFormer, IDT, DnSwin, DRSFormer, MWDCNN, WSDFormer, EWT, DECS-Net.

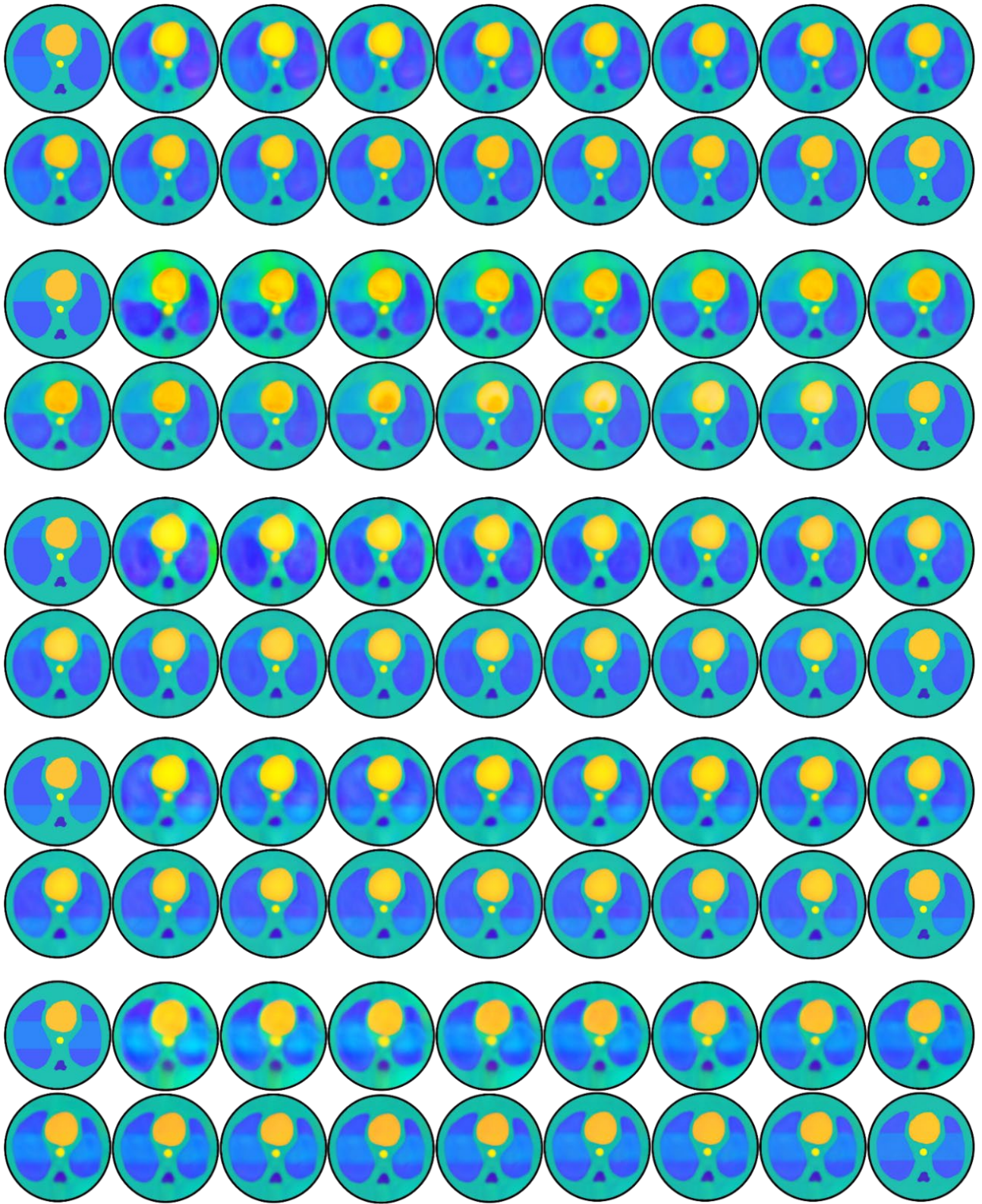


Fig. S5 The **visualizations** of reconstruction results under the *lung-shaped phantoms of simulated test datasets*. In each group, the first and second row indicate the reconstructed images, and the third and fourth row show the absolute error maps between the reconstruction and the ground truth. Here, the first image shows the ground truth distribution, and the last image shows the results of our SpW-Net, respectively. The other images are results of different comparisons including FISTA-Net, VA-Net, EED, DHU-Net, SWISTA-Net, PDCISTA-Net, SwinIR, Restormer, UFormer, IDT, DnSwin, DRSFormer, MWDCNN, WSDFormer, EWT, DECS-Net.

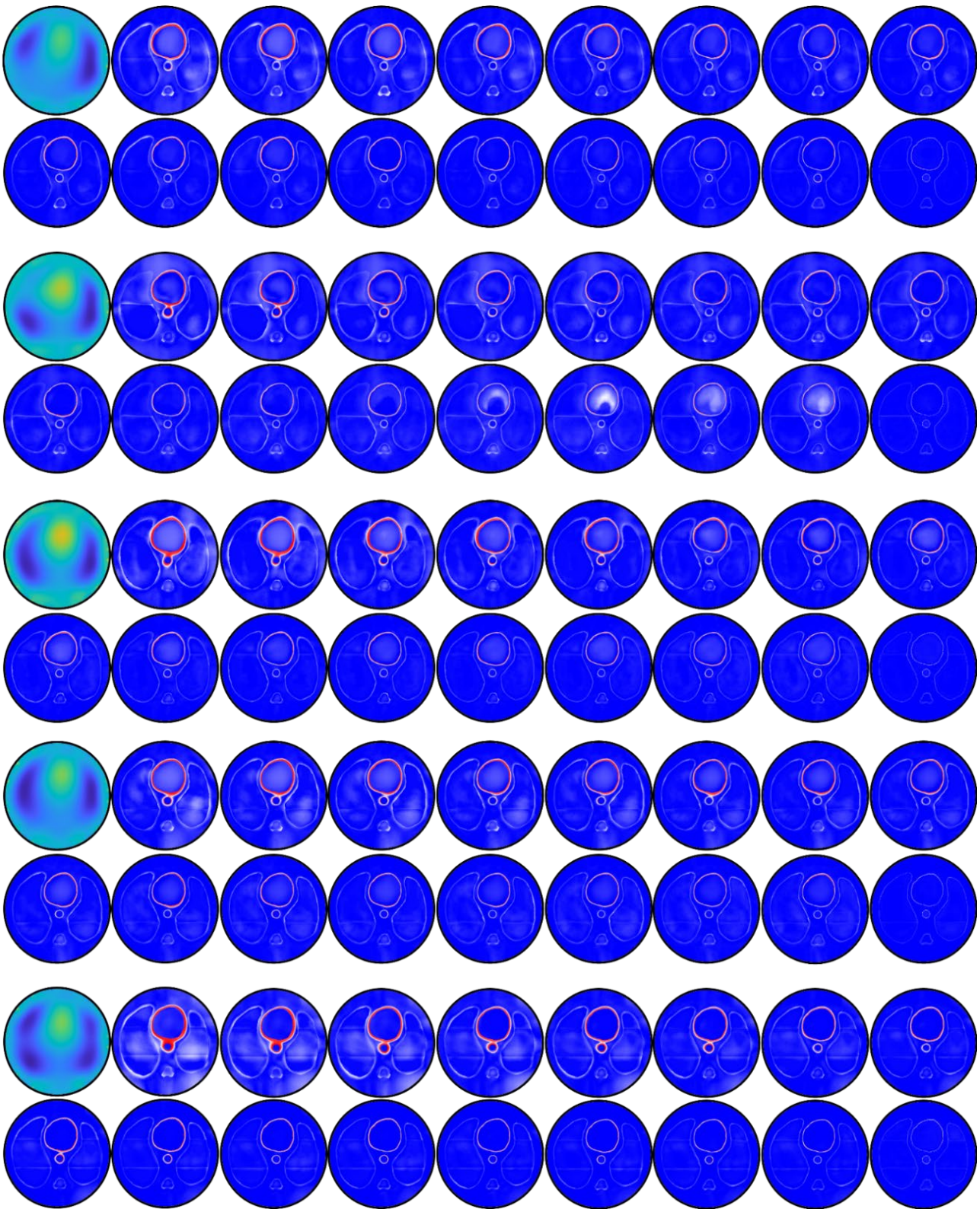


Fig. S6 The **absolute error maps** of reconstruction results under the *lung-shaped phantoms of simulated test datasets*. In each group, the first and second row indicate the reconstructed images, and the third and fourth row show the absolute error maps between the reconstruction and the ground truth. Here, the first image shows the ground truth distribution, and the last image shows the results of our SpW-Net, respectively. The other images are results of different comparisons including FISTA-Net, VA-Net, EED, DHU-Net, SWISTA-Net, PDCISTA-Net, SwinIR, Restormer, UFormer, IDT, DnSwin, DRSFormer, MWDCNN, WSDFormer, EWT, DECS-Net.

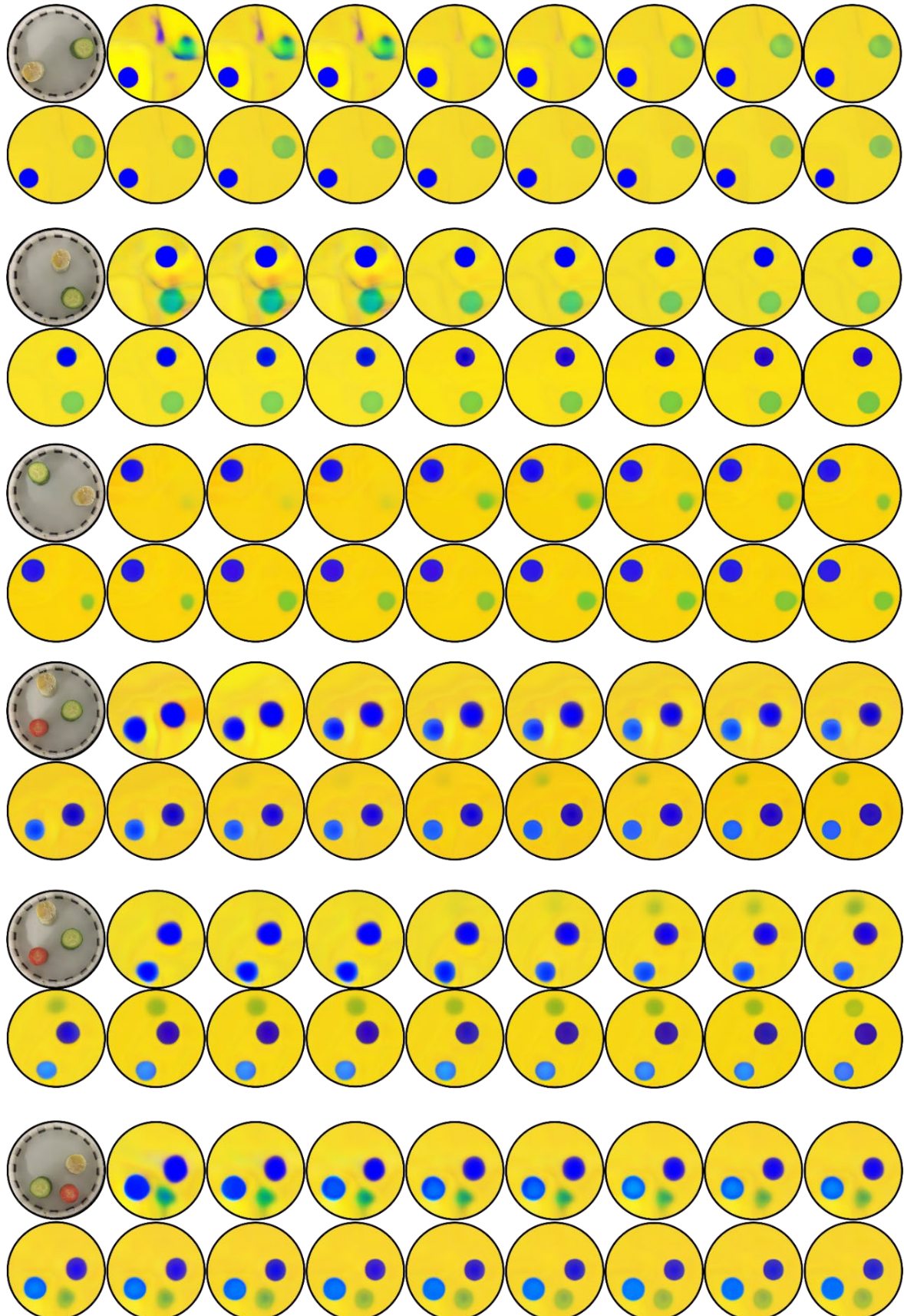


Figure S7 The visualizations of reconstruction results under the **real-world measured data *of multi-phase inclusions with two and three objects***. In each group, the first and second row indicate the reconstructed images. Here, the first image shows the ground truth distribution, and the last image shows the results of our SpW-Net, respectively. The other images are results of different comparisons including FISTA-Net, VA-Net, EED, DHU-Net, SWISTA-Net, PDCISTA-Net, SwinIR, Restormer, UFormer, IDT, DnSwin, DRSFormer, MWDCNN, WSDFormer, EWT, DECS-Net.

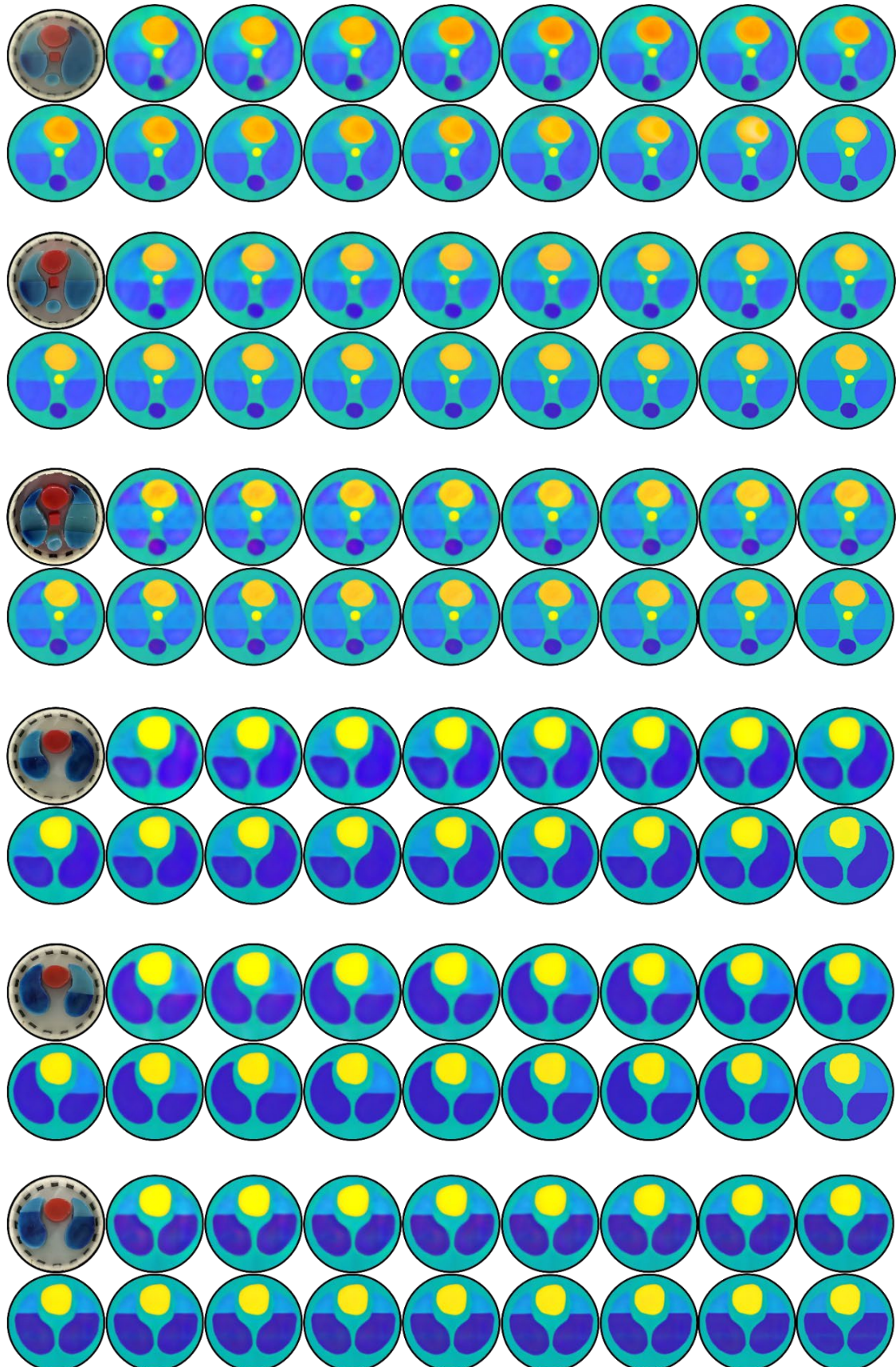


Figure S8 The visualizations of reconstruction results under the **real-world measured data of *lung-shaped phantoms including complicated shapes and multi-conductivities indicating the injured/healthy tissues***. In each group, the first and second row indicate the reconstructed images. Here, the first image shows the ground truth distribution, and the last image shows the results of our SpW-Net, respectively. The other images are results of different comparisons including FISTA-Net, VA-Net, EED, DHU-Net, SWISTA-Net, PDCISTA-Net, SwinIR, Restormer, UFormer, IDT, DnSwin, DRSFormer, MWDCNN, WSDFormer, EWT, DECS-Net.

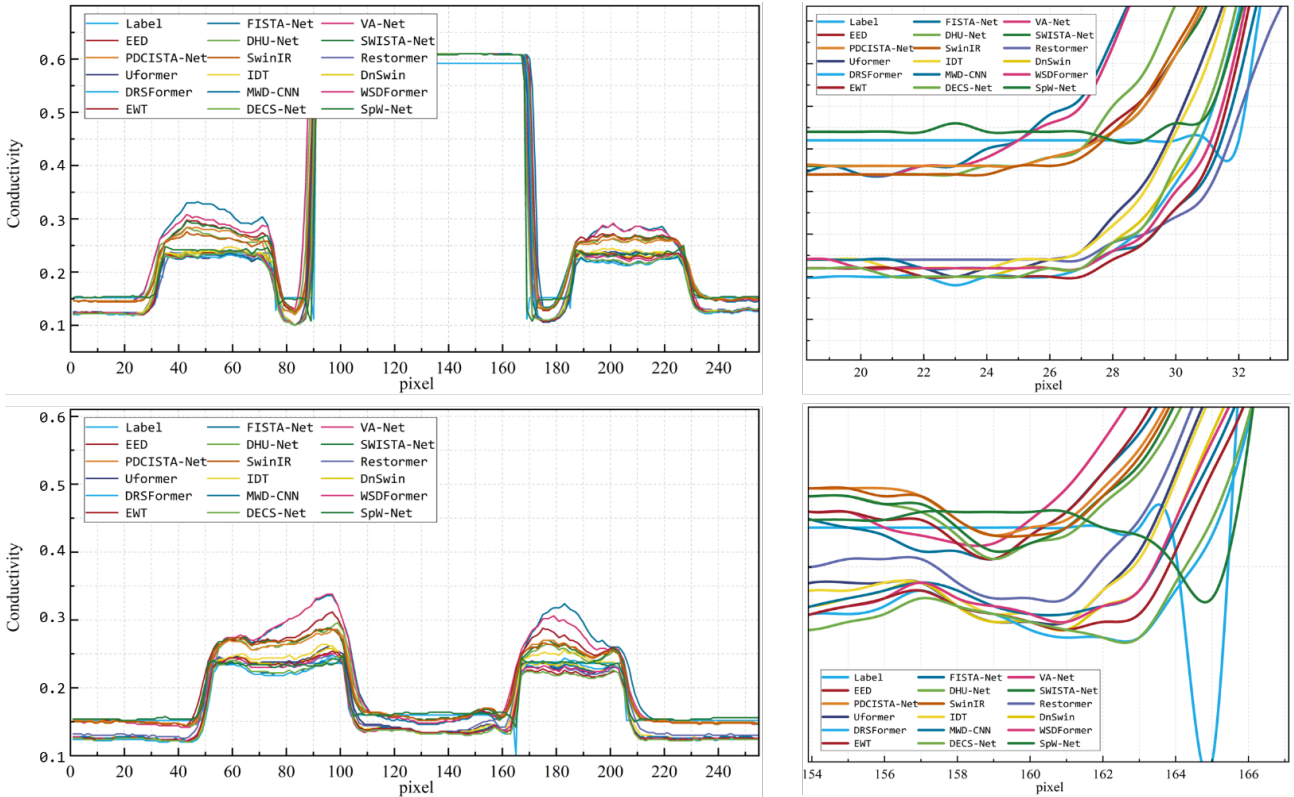


Fig. S9 The preservations of impedance-resolution performance. Here, we compare the horizontal/vertical profile of between ground truth and the reconstruction results.

## Reference:

- [1] J. Xiang, Y. Dong, and Y. Yang, "FISTA-Net: Learning a fast iterative shrinkage thresholding network for inverse problems in imaging," *IEEE Transactions on Medical Imaging*, vol. 40, no. 5, pp. 1329-1339, 2021.
- [2] Z. Wang, X. Zhang, R. Fu, D. Wang, X. Chen, and H. Wang, "Electrical impedance tomography image reconstruction with attention-based deep convolutional neural network," *IEEE Transactions on Instrumentation and Measurement*, vol. 72, pp. 1-18, 2023.
- [3] X. Tian et al., "Effective electrical impedance tomography based on enhanced encoder - decoder using atrous spatial pyramid pooling module," *IEEE Journal of Biomedical and Health Informatics*, vol. 27, no. 7, pp. 3282-3291, 2023.
- [4] Z. Wang, X. Li, Y. Sun and Q. Wang, "Electrical Impedance Tomography Deep Imaging With Dual-Branch U-Net Based on Deformable Convolution and Hyper-Convolution," in *IEEE Transactions on Instrumentation and Measurement*, vol. 73, pp. 1-16, 2024, Art no. 4503416, doi: 10.1109/TIM.2024.3369160.
- [5] B. Lu, L. Fu, Y. Pan, and Y. Dong, "SWISTA-Nets: subband-adaptive wavelet iterative shrinkage thresholding networks for image reconstruction," *Computerized Medical Imaging and Graphics*, vol. 113, p. 102345, 2024.

- 
- [6] G. Ma, H. Chen, S. Dong, X. Wang and S. Zhang, "PDCISTA-Net: Model-Driven Deep Learning Reconstruction Network for Electrical Impedance Tomography-Based Tactile Sensing," in *IEEE Transactions on Industrial Informatics*, vol. 21, no. 1, pp. 633-642, Jan. 2025, doi: 10.1109/TII.2024.3456443.
  - [7] J. Liang, J. Cao, G. Sun, K. Zhang, L. Van Gool, and R. Timofte, "Swinir: Image restoration using swin transformer," in *Proceedings of the IEEE/CVF International Conference on computer vision*, 2021, pp. 1833-1844.
  - [8] S. W. Zamir, A. Arora, S. Khan, M. Hayat, F. S. Khan, and M.-H. Yang, "Restormer: Efficient transformer for high-resolution image restoration," in *Proceedings of the IEEE/CVF conference on computer vision and pattern recognition*, 2022, pp. 5728-5739.
  - [9] Z. Wang, X. Cun, J. Bao, W. Zhou, J. Liu, and H. Li, "Uformer: A general u-shaped transformer for image restoration," in *Proceedings of the IEEE/CVF conference on computer vision and pattern recognition*, 2022, pp. 17683-17693.
  - [10] J. Xiao, X. Fu, A. Liu, F. Wu, and Z.-J. Zha, "Image de-raining transformer," *IEEE Transactions on pattern analysis and machine intelligence*, vol. 45, no. 11, pp. 12978-12995, 2022.
  - [11] H. Li et al., "DnSwin: Toward real-world denoising via a continuous Wavelet Sliding Transformer," *Knowledge-Based Systems*, vol. 255, p. 109815, 2022.
  - [12] X. Chen, H. Li, M. Li, and J. Pan, "Learning a sparse transformer network for effective image deraining," in *Proceedings of the IEEE/CVF conference on computer vision and pattern recognition*, 2023, pp. 5896-5905.
  - [13] C. Tian, M. Zheng, W. Zuo, B. Zhang, Y. Zhang, and D. Zhang, "Multi-stage image denoising with the wavelet transform," *Pattern Recognition*, vol. 134, p. 109050, 2023.
  - [14] R. Zhang, J. Yu, J. Chen, G. Li, L. Lin, and D. Wang, "A prior guided wavelet-spatial dual attention transformer framework for heavy rain image restoration," *IEEE Transactions on Multimedia*, vol. 26, pp. 7043-7057, 2024.
  - [15] J. Li, B. Cheng, Y. Chen, G. Gao, J. Shi, and T. Zeng, "EWT: Efficient wavelet-transformer for single image denoising," *Neural Networks*, vol. 177, p. 106378, 2024.
  - [16] J. Zhang, Z. Zeng, P. K. Sharma, O. Alfarraj, A. Tolba, and J. Wang, "A dual encoder crack segmentation network with Haar wavelet-based high – low frequency attention," *Expert Systems with Applications*, vol. 256, p. 124950, 2024.